

# Switchable Chern Insulators and Competing Quantum Phases in Rhombohedral Graphene Moiré Superlattices

Jian Zheng,<sup>1,†</sup> Size Wu,<sup>1,†</sup> Kai Liu,<sup>1</sup> Bosai Lyu,<sup>1</sup> Shuhan Liu,<sup>1</sup> Yating Sha,<sup>1</sup> Zhengxian Li,<sup>1</sup> Kenji Watanabe,<sup>2</sup> Takashi Taniguchi,<sup>3</sup> Jinfeng Jia,<sup>1</sup> Zhiwen Shi,<sup>1</sup> Guorui Chen<sup>1,\*</sup>

<sup>1</sup> Key Laboratory of Artificial Structures and Quantum Control (Ministry of Education), School of Physics and Astronomy and Tsung-Dao Lee Institute, Shanghai Jiao Tong University, Shanghai, China.

<sup>2</sup> Research Center for Electronic and Optical Materials, National Institute for Materials Science, 1-1 Namiki, Tsukuba 305-0044, Japan.

<sup>3</sup> Research Center for Materials Nanoarchitectonics, National Institute for Materials Science, 1-1 Namiki, Tsukuba 305-0044, Japan.

<sup>†</sup>These authors contributed equally to this work.

\*Correspondence to: chenguorui@sjtu.edu.cn

**ABSTRACT** Graphene-based moiré superlattices provide a versatile platform for exploring novel correlated and topological electronic states, driven by enhanced Coulomb interactions within flat bands. The intrinsic tunability of graphene's multiple degrees of freedom enables precise control over these complex quantum phases. In this study, we observe a range of competing phases and their transitions in rhombohedral stacked hexalayer graphene on hexagonal boron nitride (*r*-6G/hBN) moiré superlattices. When electrons are polarized away from the moiré superlattice, we firstly identify a Chern insulator with reversible Chern numbers at  $\nu = 1$  (one electron per moiré cell), revealing a competition between bulk and edge orbital magnetization. At  $\nu = 2$ , three distinct insulating phases—spin-antiferromagnetic (AFI), spin-polarized (SPI), and valley-polarized (VPI)—emerge under vertical displacement field (*D*) and magnetic field  $B_{\perp}$ , governed by hierarchical isospin symmetry breaking. Furthermore, charge density wave (CDW) states at  $\nu = 1/3$  and  $2/3$ , along with a magnetic-field-induced stripe phase at  $\nu = 1/2$ , demonstrate tunable correlated orders at fractional fillings. Our findings reveal a rich interplay of charge, isospin, topology and magnetic field in rhombohedral graphene moiré superlattices.

The exploration of correlated electronic states in solid-state systems reveals a diverse array of emergent phenomena, driven by complex interactions among electrons. Flat band systems are particularly notable in this context, as they significantly enhance Coulomb interactions by drastically reducing electron kinetic energies [1,2]. Moiré superlattices, created by stacking two-dimensional materials, provide a novel platform for engineering flat bands with multiple tunable parameters, including chemical composition, layer number, twisted angle, electrical and magnetic fields (*D* and *B*) [2–9]. Rhombohedral graphene naturally hosts flat bands, as its energy dispersion follows  $E \sim k^N$ , where *N* represents the number of layers [10–12]. As a result, Coulomb interactions strengthen when the number of layers increases, leading to the emergence of novel quantum phases, including superconductors [13,14], symmetry-broken metals [13,15–18], layer antiferromagnetic

insulators [17–21] and high order Chern insulators [22–24]. Moreover, moiré superlattice between rhombohedral graphene and hexagonal boron nitride (hBN) can further narrow the bandwidth [25,26], leading to the emergence of new exotic phases that do not exist in crystalline graphene, such as correlated insulators at integer/fractional fillings [8,27–29] and integer/fractional Chern insulators [27–29].

The emergences of correlated and topological states in graphene are often accompanied by isospin (spin and valley) polarization. A notable example is the symmetry-broken metals observed in rhombohedral multilayer graphene, which displays stoner ferromagnetism with both spin and valley polarizations [13,16–18]. The magnetism of Chern insulators in graphene-based system is also believed to originate from valley polarization [30–32]. Moreover, the sign of the orbital Chern insulator and its

magnetization can potentially be reversed when the Fermi level crosses the gap, as the total magnetization of an orbital Chern insulator arises from both bulk and edge states [30,31].

Here, we fabricated two rhombohedral stacked hexalayer graphene/hBN (*r*-6LG/hBN) moiré superlattice devices with different moiré periods (device I:  $\theta = 0.51^\circ$ , device II:  $\theta = 1.29^\circ$ ). In device I, on the positive vertical displacement field (+*D*) side, we identified a Chern insulator at filling  $\nu = 1$ , where the sign of Chern number can be tuned by doping: negative ( $C = -1$ ) under weak *p*-doping and positive ( $C = +1$ ) under weak *n*-doping. At  $\nu = 2$ , we observed two insulating states, an antiferromagnetic insulator and a spin polarized insulator, at zero magnetic field, and a valley polarized insulator in a vertical magnetic field ( $B_\perp$ ). The multiple correlated insulators here are closely tied to richer symmetry breaking metal states in crystalline *r*-6LG compared to thinner layer rhombohedral graphene. In device II, on the negative vertical displacement field (-*D*) side, charge density wave (CDW) insulating phases with different spin textures were observed at fractional fillings of 1/3 and 2/3. Under a vertical magnetic field, a stripe phase appears at  $\nu = 1/2$ . The onsite *D* of the fractional insulating states shows a linear dependence with the magnetic flux of the CDW/stripe unit cell, indicating the role of magnetic field to the moiré bandwidth.

Figure 1(a) depicts a schematic cross-sectional view of the device, showcasing a dual gate structure that enables independent tuning of carrier density *n* and the vertical displacement field *D*. To eliminate any possible moiré superlattice between *r*-6LG and top hBN, monolayer tungsten disulfide (WS<sub>2</sub>) is used as a spacer. Consequently, the moiré superlattice arises solely from the alignment between *r*-6LG and bottom hBN. The optical image of device I is shown in Fig. S1 [33], with a moiré period of  $L = 13.4$  nm and a twist angle of  $\theta = 0.51^\circ$ , as confirmed by the carrier concentration of the resistance peaks at integer fillings, and the carrier concentration is confirmed by the Landau fan diagram (Fig. S2 in the Supplemental Material [33]). Figure 1(b) shows the four-probe resistance  $R_{xx}$  of device I as functions of  $\nu$  and *D*. Line plots of  $R_{xx}$  at different *D* is shown in Fig. 1(c). As *D* is applied in either direction, the resistance at  $\nu = 0$  increases due to band gap opening. Upon electron doping, four resistance peaks are well developed on the -*D* side at integer fillings of  $\nu = 1, 2, 3$ , and 4, whereas on the +*D* side, resistance peaks appear only at  $\nu = 1$  and 2. The resistance peaks at  $\nu = 4$  corresponds to full filling of the first conduction miniband, while other insulating peaks at integer fillings from 1 to 3 arises from correlations. The asymmetry between +*D* and -*D* side stems from different strength of moiré potential experienced by

the electrons in the top and bottom graphene layers. On the -*D* side, the electrons are closer to the moiré superlattice and experiences stronger moiré modulation, while on the +*D* side, electrons are polarized toward the top graphene layer, moving away from the moiré superlattice. This is further evidenced by clear phase boundaries between isospin-polarized metals on the +*D* side. While the phase boundaries are almost absent due to strong moiré modulations on the -*D* side. Notably, no insulating peaks are observed on the hole-doping side within the range of *D* explored in our experiment. The electron-hole asymmetry can be explained by the wider bandwidth on the hole side relative to the electron side in the *r*-6LG/hBN moiré superlattice [34–36].

On the +*D* side, the  $\nu = 1$  correlated insulator is predicted to be topological Chern insulator with a Chern number of  $C = 1$  [34–38]. Interestingly, however, we initially observe a  $C = -1$  Chern insulator at this filling in our device. Figures 2(a) and (b) present the longitudinal resistance  $R_{xx}$  and Hall resistance  $R_{xy}$  as functions of  $\nu$  and *D* at  $B_\perp = 1$  T. On either doping side of the  $\nu = 1$  insulating peak, dips in  $R_{xx}$  are evident, as indicated by the dashed lines in Fig. 2(a). In the same region (indicated by dashed lines in Fig. 2(b)), large Hall signals are observed, but with different signs for hole- and electron-doping (Figs. 2(b) and S4 in the Supplemental Material [33]). Fixing the doping on the hole side of the  $\nu = 1$  insulator at  $D = 0.65$  V/nm, we observe a pronounced anomalous Hall signal in  $R_{xy}$  upon sweeping  $B_\perp$ , as shown in Fig. 2(e). The anomalous Hall resistance reaches 15 k $\Omega$  at zero magnetic field, and from the sign of  $R_{xy}$  at positive and negative magnetic fields, we determine the Chern number to be  $C = -1$ . When the moiré superlattice is slightly doped on the electron side of the  $\nu = 1$  insulator, an anomalous Hall signal with same sign is detected near zero magnetic field (Fig. 2(f)). With increasing magnetic field,  $R_{xy}$  reverses its sign, and  $R_{xy}$  reach the quantized value of  $h/e^2$  at 2.5 T, corresponding to the predicted  $C = 1$  Chern insulator. The development of the  $C = \pm 1$  Chern insulator is more clearly illustrated in the Landau fan diagram (Figs. 2(c) and (d)), where both Chern insulating states ( $C = \pm 1$ ) disperse with increasing  $B_\perp$ , consistent with the Streda's formula (marked by the two black dashed lines). These observations suggest that the Chern insulator here is *n*-dependent, and its sign can be reversed by tuning the doping. Same measurements at  $D = 0.62$  V/nm and  $D = 0.7$  V/nm reveal the same sign-reversal behavior (Fig. S5 in the Supplemental Material [33]). As shown in Figs. 2(a) and (b), Chern insulating states with opposite signs start to appear at  $D = 0.55$  V/nm, and persists up to 0.73 V/nm, the highest *D* applied in our experiment.

The doping-induced sign reversal of Chern number  $C$  is related to the sign change in total magnetization  $M$ . In an orbital Chern insulator, the total magnetization  $M$  arises from both bulk  $M_{\text{bulk}}$  and edge state  $M_{\text{edge}}$ . If  $M_{\text{edge}}$  is large enough, then  $M$  can change sign as the Fermi level crosses the gap [23,30,31]. The evolution of Chern insulator in magnetic field can be understood by the relationship between  $C$  and  $M$ . If  $M$  does not change sign across the gap and  $C_{\pm}M_{\pm} > 0$  ( $C_{\pm}M_{\pm} < 0$ ), the magnetic field stabilizes the positive (negative)  $C$  for positive  $B$  and the negative (positive)  $C$  for negative  $B$ . In the  $r$ -6LG/hBN superlattice,  $M$  changes sign across the gap, making both signs ( $\pm$ ) of the Chern insulator robust in a magnetic field. Detailed illustrations for the three cases have been discussed in the supplementary material of Ref 30 and are also provided in Fig. S6 [33].

At  $\nu = 2$ , the correlated insulator is generally believed to be topological trivial because it does not occupy a pure valley. Indeed, we do not see any anomalous hall signal near  $\nu = 2$ . However, as shown in Figs. 1(b) and (c), there are two insulating regions at  $\nu = 2$ : one from 0.1 V/nm to 0.18 V/nm, the other from 0.4 V/nm to 0.74 V/nm. For comparison, in rhombohedral trilayer to pentalayer moiré superlattices, only one insulating phase emerge at  $\nu = 2$  [8,29,36]. Figure 3(a) shows a line cut at  $\nu = 2$  along  $D$  axis, where the insulating states are labeled as I and II, respectively. We attribute this  $D$ -induced two correlated insulator to rich isospin competitions in crystalline hexalayer graphene. In order to determine the isospin flavors in these two insulating states, we applied perpendicular and parallel magnetic fields  $B_{\perp}$  and  $B_{\parallel}$  with respect to graphene plane, because valley only responds to  $B_{\perp}$  and spin equally responds to  $B_{\perp}$  and  $B_{\parallel}$ . The resulting  $D - B_{\perp}$  and  $D - B_{\parallel}$  maps of  $R_{xx}$  are shown in Figs. 3(b) and (c), respectively. Both insulators I and II are suppressed with increasing  $B_{\perp}$ , with insulator I persisting up to  $B_{\perp} = 2.1$  T and insulator II up to  $B_{\perp} = 6.5$  T. However, the two insulators exhibit opposite responses to  $B_{\parallel}$ : insulator I is suppressed, while insulator II is enhanced. Remarkably, a new high-resistance state labeled as III emerges at higher  $D$  as  $B_{\perp}$  increases, which is separated by a phase boundary from the insulator II.

To quantitatively compare these insulating states, we varied the temperature and estimated their transport gap. Fig. 3(d) shows the evolution of the transport gaps of the three insulating states as a function of  $B_{\parallel}$  or  $B_{\perp}$ . At zero magnetic field, the gap size of insulator I is approximately 2.9 meV ( $D = 0.14$  V/nm), and that of insulator II is about 0.88 meV ( $D = 0.48$  V/nm). As  $B_{\parallel}$  increases, the gap of the insulator I decreases linearly, following the Zeeman energy  $g_I \mu_B B_{\parallel}$ , with an estimated g-factor of  $g_I \approx 2$ . In

contrast, the gap of the insulator II increases linearly with  $B_{\parallel}$ , also following the Zeeman energy  $g_{II} \mu_B B_{\parallel}$ , with an estimated g-factor of  $g_{II} \approx 2$ . These observations suggest that insulator I is an antiferromagnetic insulator (AFI), and the insulator II is a spin polarized insulator (SPI). For the insulator III, the gap size (at  $D = 0.60$  V/nm) increases linearly with  $B_{\perp}$ , following  $g_{III} \mu_B B_{\perp}$  with an estimated g-factor of  $g_{III} = 9$ . This large g factor suggests that valley plays a more substantial role than spin in insulator III. Thus, insulator III is identified as a valley polarized insulator (VPI).

These insulating phases at  $\nu = 2$  is schematically illustrated in Fig. 3(e), which shows the isospin ground states for the three insulators. We further compared these insulators at  $\nu = 2$  with the isospin symmetry-broken metals in crystalline  $r$ -6LG (Fig. S3 in the Supplemental Material [33]) without moiré. We find that the SPI state is situated in the spin polarized half-metal region, the VPI state is in the valley polarized quarter-metal region, and the AFI state lies at the phase boundary between normal metal and half-metal regions. The correspondence suggests that novel correlated insulator phases can be expected in thicker rhombohedral graphene moiré superlattices where isospin metal phases become more complexed.

We measured a second device with smaller moiré period  $L = 8.93$  nm and larger twist angle  $\theta = 1.29^\circ$ . The transport data of this device, shown in Fig. 4(a), reveal several differences from the first device. First, at  $\nu = 0$ , the layer antiferromagnetic (LAF) insulator at  $D = 0$  V/nm survives, similar to that observed in crystalline  $r$ -6LG without moiré (Fig. S3 in the Supplemental Material [33]). Second, the AFI state (insulator I) at  $\nu = 2$  is absent. Third, other integer filling insulators in this device emerge at higher  $D$  values, and the phase boundaries between isospin-polarized metals are distinct for both directions of  $D$ . These differences are due to the weaker moiré modulations in the device with larger twist angle.

Besides these notable differences, there is a tilted stripe-shaped high resistance region at  $-D$  side ( $-0.95$  V/nm  $\sim -0.75$  V/nm) between  $\nu = 0$  and 1. Figure 4(b) presents a zoomed-in view of this region, where two resistance peaks at fractional fillings  $\nu = 1/3$  and  $2/3$  are clearly resolved. These two insulating states are referred to charge density wave (CDW). The transport gaps of these two CDW states are about 0.85 meV and 0.57 meV, respectively, based on the temperature-dependent measurements (Fig. S7 in the Supplemental Material [33]). Interestingly, under  $B_{\perp}$ , these two CDW states shifts to smaller  $|D|$ . Starting from  $B_{\perp} = 5$  T, a new resistance peak at  $\nu = 1/2$  starts to appear and is further prominent under higher  $B_{\perp}$  (Fig. 4(c)). The state at  $\nu = 1/2$  breaks  $C_3$  symmetry of the moiré superlattice, and is referred as a stripe phase

insulator. We extracted the  $D$  and  $B_{\perp}$  values of the maximum resistances, and plotted  $D$  vs magnetic flux per CDW/stripe unit cell  $\Phi = B_{\perp} \cdot A$ , where  $A$  is three and two times of moiré superlattice unit cell for  $\nu = 1/3$  ( $2/3$ ) and  $1/2$ , respectively, in Fig. 4(d). Surprisingly, all fractional states exhibit linear relation with the same slope. The effect of  $\Phi$  is possibly to reduce the moiré bandwidth by adding an extra term in the hopping energy between CDW/stripe site, and therefore decreasing the onset  $D$  (Fig. S8 in the Supplemental Material [33]).

Under increasing  $B_{\parallel}$ ,  $1/3$  and  $2/3$  CDW states exhibit opposite behaviors. At  $D = -0.85$  V/nm,  $1/3$  CDW state is well-developed while  $2/3$  state is absent (Fig. 4(b)). As  $B_{\parallel}$  increases, the resistance of  $1/3$  state decreases, eventually disappearing around  $B_{\parallel} = 10$  T (Fig. S9(a) in the Supplemental Material [33]), while the  $2/3$  state appears near 5 T. At  $D = -0.88$  V/nm, the  $2/3$  state is well-developed at zero magnetic field (Fig. 4(b)) and its resistance increases with  $B_{\parallel}$ , whereas the  $1/3$  state remain absent at  $B_{\parallel} = 12$  T (Fig. S9(b) in the Supplemental Material [33]). This contrasting dependence on  $B_{\parallel}$  suggests distinct spin textures of the  $1/3$  and  $2/3$  CDW states.

At last, we note that the LAF state is absent in device I and present in device II. We attribute the absence of LAF state in device I to the moiré-induced imbalance between the top and bottom graphene layers. Previous investigations have shown that graphene/hBN moiré superlattice ( $L = 13.5$  nm) can create large band gap about 25 meV at  $\nu = 0$  [38]. This

energy scale agrees with the gap size of LAF state in crystalline  $r$ -6LG, which is about 27 meV (Fig. S3(d) in the Supplemental Material [33]).

In summary, we report the observation of a variety of topological and correlated phase in  $r$ -6LG/hBN moiré superlattice on both sides of  $D$ . On the  $+D$  side, we identify a switchable Chern insulator at filling  $\nu = 1$ . At  $\nu = 2$ , we observe three insulating phases with isospin competitions, which can be controlled by  $D$  and  $B$ . Additionally, correlated insulators at fractional fillings of  $1/3$ ,  $1/2$  and  $2/3$  emerge at  $-D$  side. These findings unveil a wealth of correlated and topological phases with multiple competing orders and tuning parameters in rhombohedral multilayer graphene moiré superlattices. Our results showcase moiré superlattice as a condensed matter quantum simulator, offering a versatile platform for the realization and precise tuning of diverse quantum states.

## ACKNOWLEDGMENTS

This work is supported by NSF of China (grant nos. 12350005 and 12174248), National Key Research Program of China (grant nos. 2021YFA1400100 and 2020YFA0309000), and Shanghai Science and Technology Innovation Action Plan (grant no. 24LZ1401100). G.C. acknowledges support from Yangyang Development Fund. K.W. and T.T. acknowledge support from the JSPS KAKENHI (Grant Numbers 20H00354, 21H05233 and 23H02052) and World Premier International Research Center Initiative (WPI), MEXT, Japan.

- 
- |  |   |
|--|---|
| <p>[1] S. Paschen and Q. Si, Quantum phases driven by strong correlations, <i>Nat Rev Phys</i> <b>3</b>, 9 (2020).</p> <p>[2] K. P. Nuckolls and A. Yazdani, A microscopic perspective on moiré materials, <i>Nat Rev Mater</i> <b>9</b>, 460 (2024).</p> <p>[3] T. Li et al., Quantum anomalous Hall effect from intertwined moiré bands, <i>Nature</i> <b>600</b>, 641 (2021).</p> <p>[4] R. Bistritzer and A. H. MacDonald, Moiré bands in twisted double-layer graphene, <i>Proc. Natl. Acad. Sci. U.S.A.</i> <b>108</b>, 12233 (2011).</p> <p>[5] Y. Cao et al., Correlated insulator behaviour at half-filling in magic-angle graphene superlattices, <i>Nature</i> <b>556</b>, 80 (2018).</p> <p>[6] Y. Cao, V. Fatemi, S. Fang, K. Watanabe, T. Taniguchi, E. Kaxiras, and P. Jarillo-Herrero, Unconventional superconductivity in magic-angle graphene superlattices, <i>Nature</i> <b>556</b>, 43 (2018).</p> <p>[7] Y. Cao, D. Rodan-Legrain, O. Rubies-Bigorda, J. M. Park, K. Watanabe, T. Taniguchi, and P. Jarillo-Herrero, Tunable correlated states and</p> | <p>spin-polarized phases in twisted bilayer-bilayer graphene, <i>Nature</i> <b>583</b>, 215 (2020).</p> <p>[8] G. Chen et al., Evidence of a gate-tunable Mott insulator in a trilayer graphene moiré superlattice, <i>Nat. Phys.</i> <b>15</b>, 237 (2019).</p> <p>[9] E. C. Regan et al., Mott and generalized Wigner crystal states in WSe<sub>2</sub>/WS<sub>2</sub> moiré superlattices, <i>Nature</i> <b>579</b>, 359 (2020).</p> <p>[10] C. Yelgel, Electronic Structure of ABC-stacked Multilayer Graphene and Trigonal Warping: A First Principles Calculation, <i>J. Phys.: Conf. Ser.</i> <b>707</b>, 012022 (2016).</p> <p>[11] M. Koshino and E. McCann, Trigonal warping and Berry's phase <math>N\pi</math> in ABC-stacked multilayer graphene, <i>Phys. Rev. B</i> <b>80</b>, 165409 (2009).</p> <p>[12] H. Min and A. H. MacDonald, Electronic Structure of Multilayer Graphene, <i>Prog. Theor. Phys. Suppl.</i> <b>176</b>, 227 (2008).</p> <p>[13] H. Zhou, L. Holleis, Y. Saito, L. Cohen, W. Huynh, C. L. Patterson, F. Yang, T. Taniguchi, K. Watanabe, and A. F. Young, Isospin</p> |
|--|---|

- magnetism and spin-polarized superconductivity in Bernal bilayer graphene, *Science* **375**, 774 (2022).
- [14] H. Zhou, T. Xie, T. Taniguchi, K. Watanabe, and A. F. Young, Superconductivity in rhombohedral trilayer graphene, *Nature* **598**, 434 (2021).
- [15] T. Han et al., Orbital multiferroicity in pentalayer rhombohedral graphene, *Nature* **623**, 41 (2023).
- [16] H. Zhou et al., Half- and quarter-metals in rhombohedral trilayer graphene, *Nature* **598**, 429 (2021).
- [17] T. Han, Z. Lu, G. Scuri, J. Sung, J. Wang, T. Han, K. Watanabe, T. Taniguchi, H. Park, and L. Ju, Correlated insulator and Chern insulators in pentalayer rhombohedral-stacked graphene, *Nat. Nanotechnol.* **19**, 181 (2024).
- [18] K. Liu et al., Spontaneous broken-symmetry insulator and metals in tetralayer rhombohedral graphene, *Nat. Nanotechnol.* **19**, 188 (2024).
- [19] J. Velasco et al., Transport spectroscopy of symmetry-broken insulating states in bilayer graphene, *Nature Nanotech* **7**, 156 (2012).
- [20] R. T. Weitz, M. T. Allen, B. E. Feldman, J. Martin, and A. Yacoby, Broken-Symmetry States in Doubly Gated Suspended Bilayer Graphene, *Science* **330**, 812 (2010).
- [21] B. E. Feldman, J. Martin, and A. Yacoby, Broken-symmetry states and divergent resistance in suspended bilayer graphene, *Nature Phys* **5**, 889 (2009).
- [22] F. R. Geisenhof, F. Winterer, A. M. Seiler, J. Lenz, T. Xu, F. Zhang, and R. T. Weitz, Quantum anomalous Hall octet driven by orbital magnetism in bilayer graphene, *Nature* **598**, 53 (2021).
- [23] Y. Sha, J. Zheng, K. Liu, H. Du, K. Watanabe, T. Taniguchi, J. Jia, Z. Shi, R. Zhong, and G. Chen, Observation of a Chern insulator in crystalline ABCA-tetralayer graphene with spin-orbit coupling, *Science* **384**, 414 (2024).
- [24] T. Han et al., Large quantum anomalous Hall effect in spin-orbit proximitized rhombohedral graphene, *Science* **384**, 647 (2024).
- [25] Y. Park, Y. Kim, B. L. Chittari, and J. Jung, Topological flat bands in rhombohedral tetralayer and multilayer graphene on hexagonal boron nitride moiré superlattices, *Phys. Rev. B* **108**, 155406 (2023).
- [26] B. L. Chittari, G. Chen, Y. Zhang, F. Wang, and J. Jung, Gate-Tunable Topological Flat Bands in Trilayer Graphene Boron-Nitride Moiré Superlattices, *Phys. Rev. Lett.* **122**, 016401 (2019).
- [27] J. Xie et al., Even- and Odd-denominator Fractional Quantum Anomalous Hall Effect in Graphene Moiré Superlattices, (n.d.).
- [28] G. Chen et al., Magnetic Field-Stabilized Wigner Crystal States in a Graphene Moiré Superlattice, *Nano Lett.* **23**, 7023 (2023).
- [29] Z. Lu, T. Han, Y. Yao, A. P. Reddy, J. Yang, J. Seo, K. Watanabe, T. Taniguchi, L. Fu, and L. Ju, Fractional quantum anomalous Hall effect in multilayer graphene, *Nature* **626**, 759 (2024).
- [30] J. Zhu, J.-J. Su, and A. H. MacDonald, Voltage-Controlled Magnetic Reversal in Orbital Chern Insulators, *Phys. Rev. Lett.* **125**, 227702 (2020).
- [31] H. Polshyn et al., Electrical switching of magnetic order in an orbital Chern insulator, *Nature* **588**, 66 (2020).
- [32] G. Chen et al., Tunable correlated Chern insulator and ferromagnetism in a moiré superlattice, *Nature* **579**, 56 (2020).
- [33] See Supplemental Material [url] for measurement details and additional experimental data.
- [34] J. Dong, T. Wang, T. Wang, T. Soejima, M. P. Zaletel, A. Vishwanath, and D. E. Parker, Anomalous Hall Crystals in Rhombohedral Multilayer Graphene. I. Interaction-Driven Chern Bands and Fractional Quantum Hall States at Zero Magnetic Field, *Phys. Rev. Lett.* **133**, 206503 (2024).
- [35] B. Zhou, H. Yang, and Y.-H. Zhang, Fractional Quantum Anomalous Hall Effect in Rhombohedral Multilayer Graphene in the Moiréless Limit, *Phys. Rev. Lett.* **133**, 206504 (2024).
- [36] Z. Dong, A. S. Patri, and T. Senthil, Theory of Quantum Anomalous Hall Phases in Pentlayer Rhombohedral Graphene Moiré Structures, *Phys. Rev. Lett.* **133**, 206502 (2024).
- [37] Y. Choi et al., Superconductivity and quantized anomalous Hall effect in rhombohedral graphene, *Nature* **639**, 342 (2025).
- [38] B. Hunt et al., Massive Dirac Fermions and Hofstadter Butterfly in a van der Waals Heterostructure, *Science* **340**, 1427 (2013).

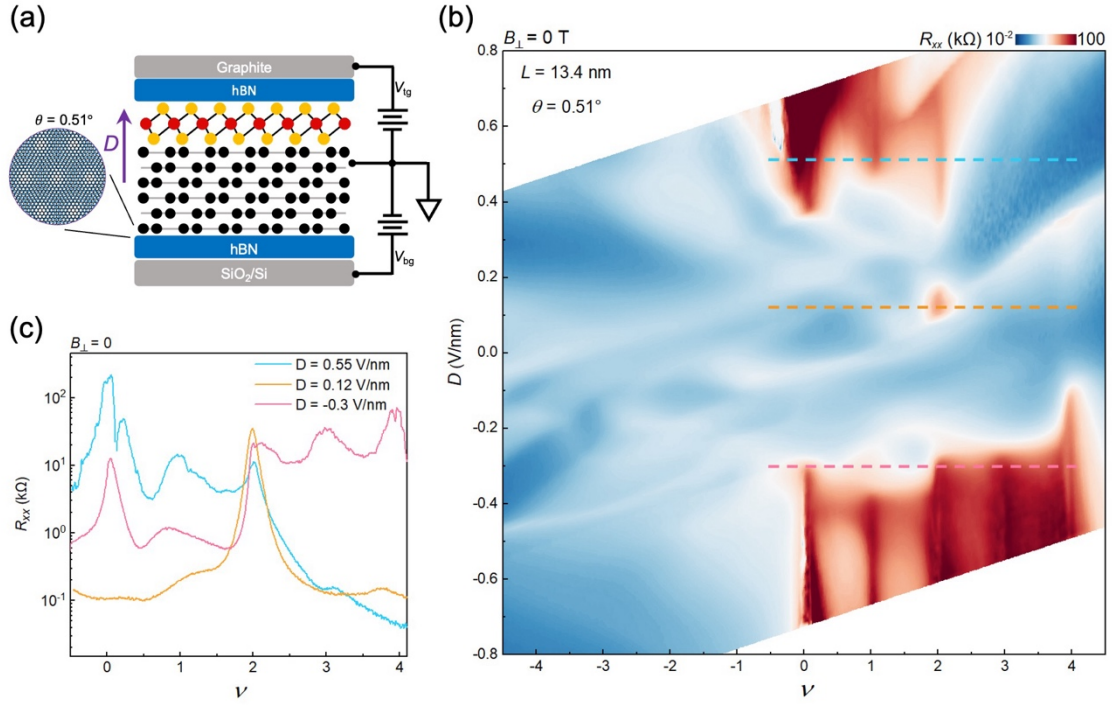


FIG. 1. (a) Schematic cross-sectional view of the device. The *r*-6LG is encapsulated in hBN flakes, forming a moiré superlattice with a period of  $L = 13.4$  nm and  $\theta = 0.51^\circ$  between *r*-6LG and bottom hBN. Monolayer WS<sub>2</sub> is used as a spacer to exclude possible effects from the moiré superlattice between *r*-6LG and top hBN. (b) Color plot of the four-probe resistance  $R_{xx}$  as functions of  $\nu$  and  $D$  at zero magnetic field. (c)  $R_{xx}$  as a function of  $\nu$  at  $D = 0.55$  V/nm,  $0.12$  V/nm, and  $-0.3$  V/nm, corresponding to the dashed lines in Fig. 1(b).

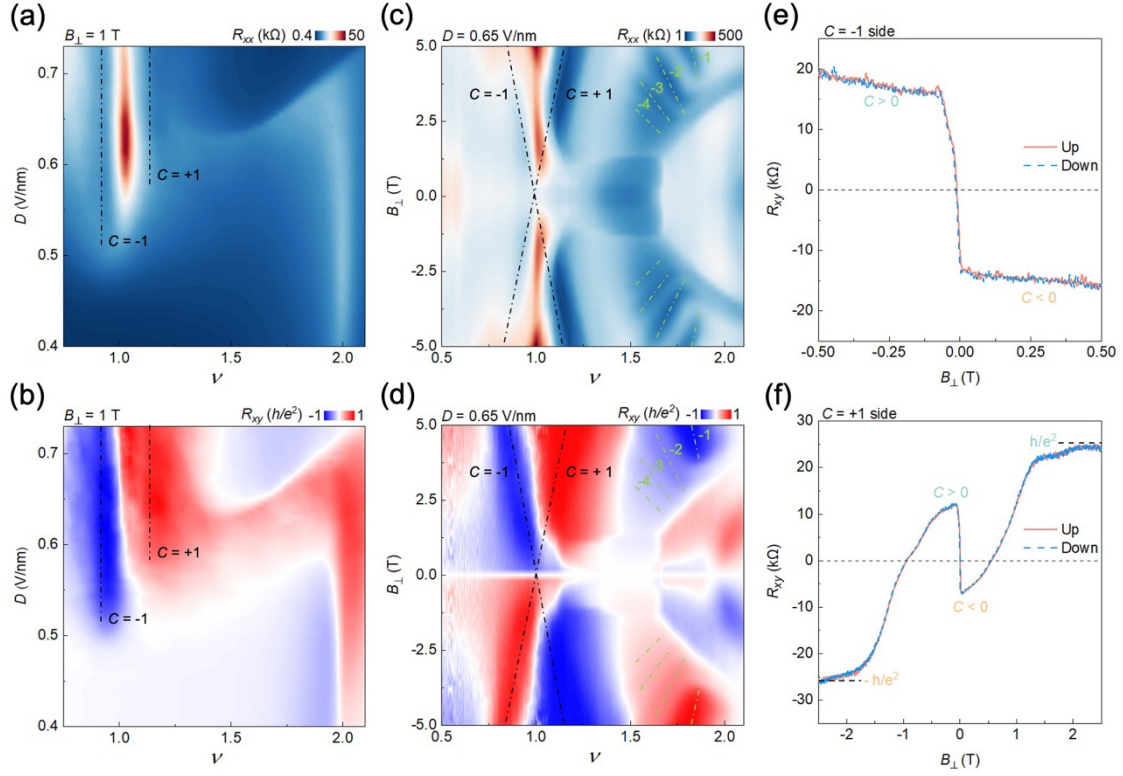


FIG. 2. (a) and (b) Color plots of  $R_{xx}$  (a) and  $R_{xy}$  (b) as functions of  $\nu$  and  $D$  at  $B_{\perp} = 1$  T. Dashed lines indicate the Chern insulator at hole ( $C = -1$ ) and electron ( $C = +1$ ) doping sides. (c) and (d) Landau fan diagrams of symmetrized  $R_{xx}$  (c) and anti-symmetrized  $R_{xy}$  (d) as functions of  $\nu$  and  $B_{\perp}$  at  $D = 0.65$  V/nm. The Chern insulators with  $C = \pm 1$  at  $\nu = 1$  are highlighted by black dashed lines, which follows the Streda formula. Landau level-induced quantum Hall states are labeled by green dashed lines with filling factors of -1, -2, -3, and -4. (e) and (f) Anomalous Hall signals  $R_{xy}$  at  $C = -1$  ( $\nu = 0.95$ ) side (e) and  $C = +1$  ( $\nu = 1.05$ ) side (f).

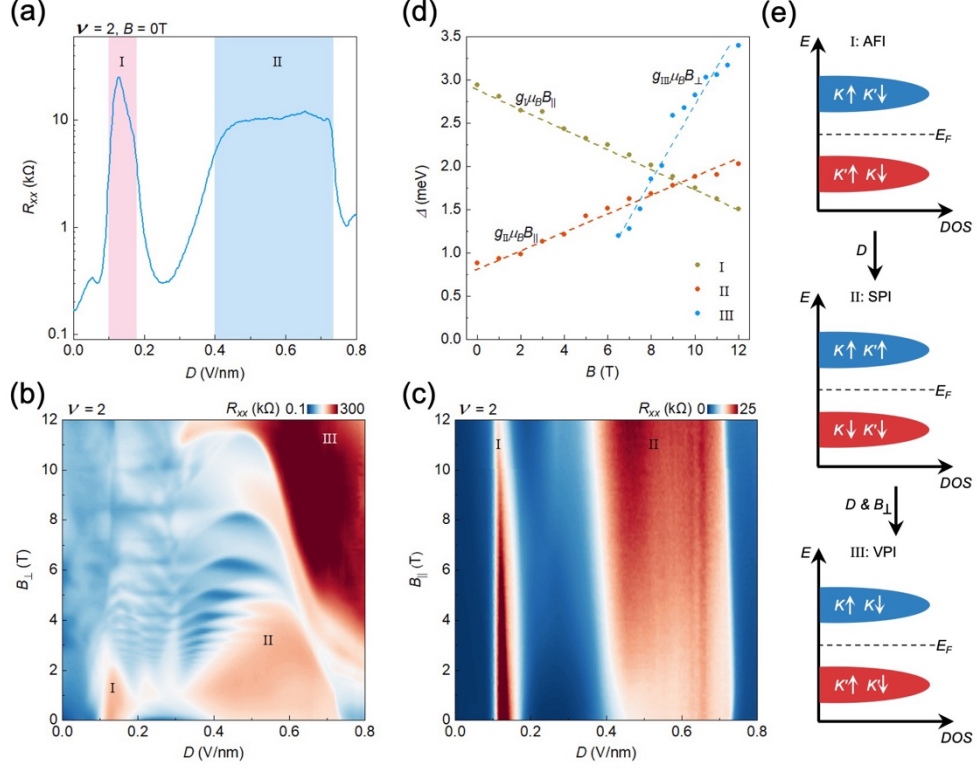


FIG. 3. (a)  $R_{xx}$  as a function of  $D$  at  $\nu = 2$ . The two insulating states at different  $D$  are labelled as I and II, respectively. (b) and (c) Color plots of  $R_{xx}$  at  $\nu = 2$  as functions of  $D$  and  $B_{\perp}$  (b) and  $B_{\parallel}$  (c).  $R_{xx}$  of insulator I decreases with both  $B_{\perp}$  and  $B_{\parallel}$ . In contrast,  $R_{xx}$  of insulator II decreases with  $B_{\perp}$  but increases with  $B_{\parallel}$ . As  $B_{\perp}$  increases, a new insulating phase gradually develops at higher  $D$ , which is labeled as III. (d) Transport gaps  $\Delta$  of the three insulators as a function of  $B_{\parallel}$  (for I and II) or  $B_{\perp}$  (for III). (e) Schematic illustration of the isospin flavor evolution for the three insulating states. The x-axis represents the density of states (DOS), the y-axis represents energy,  $E_F$  denotes the Fermi level,  $K$  and  $K'$  represents two valleys, and  $\uparrow$  and  $\downarrow$  represents two spins.

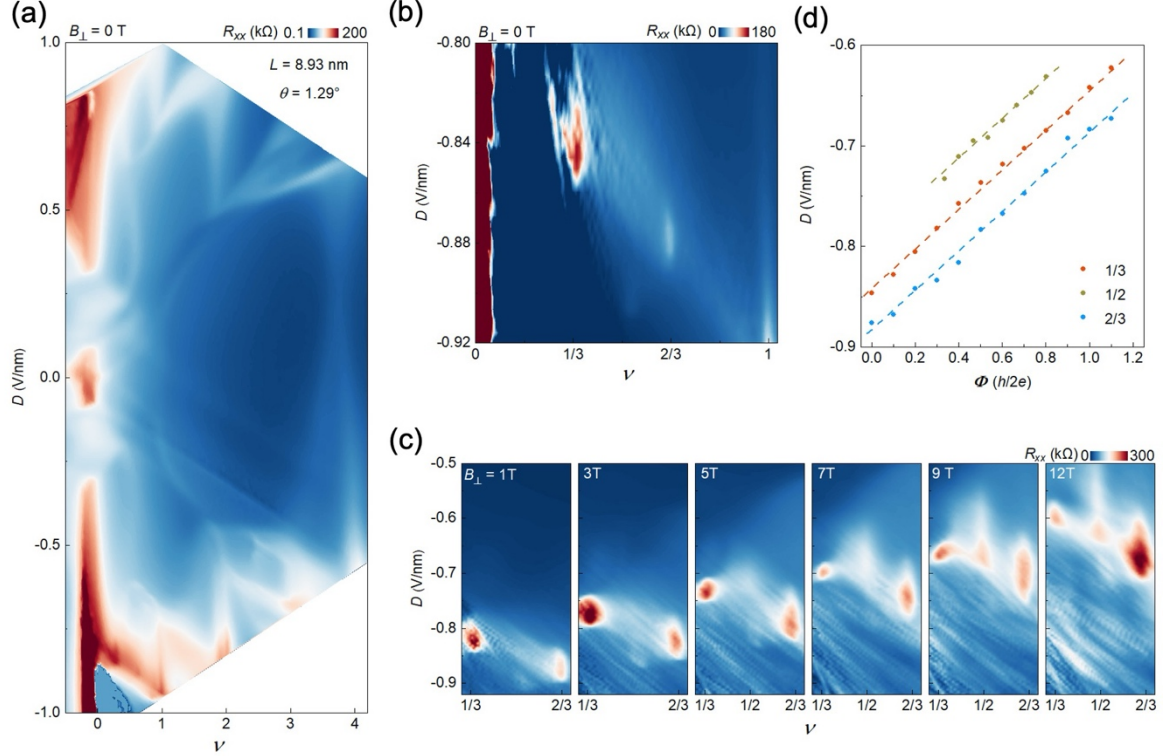


FIG. 4. (a) Color plot of  $R_{xx}$  as functions of  $\nu$  and  $D$ . This device has a moiré period of  $L = 8.93$  nm,  $\theta = 1.29^{\circ}$ . (b) Zoomed in color plot of  $R_{xx}$  at  $-D$  and  $0 < \nu < 1$ . CDW states develop at fractional fillings  $1/3$  and  $2/3$ . (c) Evolutions of CDW states under increasing  $B_{\perp}$ . As  $B_{\perp}$  increases, the CDW states shift to smaller  $D$ . At about 5T, a stripe phase appears at  $\nu = 1/2$ . (d)  $D$  as a function of  $\Phi$  for three insulating states at fractional fillings. The straight dashed lines are in the same slope.